Silver Nanoparticles' Localized Surface Plasmon Resonances Emerged in Polymeric Environments: Theory and Experiment

Maria Tsarmpopoulou [1,*], Dimitrios Ntemogiannis [1], Alkeos Stamatelatos [1,†], Dimitrios Geralis [1], Vagelis Karoutsos [1], Mihail Sigalas [1], Panagiotis Poulopoulos [1] and Spyridon Grammatikopoulos [1,2,*]

[1] Department of Materials Science, University of Patras, 26504 Patras, Greece; d.ntemogiannis@upnet.gr (D.N.); a.stamatelatos@upnet.gr (A.S.); msci921@upnet.gr (D.G.); vkar@upatras.gr (V.K.); sigalas@upatras.gr (M.S.); poulop@upatras.gr (P.P.)

[2] Department of Mechanical Engineering, University of Peloponnese, M. Alexandrou 1, 26334 Patras, Greece

[*] Correspondence: mtsarmpopo@upatras.gr (M.T.); spiridongramma@upatras.gr (S.G.); Tel.: +30-2610996383 (M.T.); +30-2610369282 (S.G.)

[†] Current address: Department of Physics, University of Warwick, Coventry CV4 7AL, UK.

Abstract: Considering that the plasmonic properties of metallic nanoparticles (NPs) are strongly influenced by their dielectric environment, comprehension and manipulation of this interplay are crucial for the design and optimization of functional plasmonic systems. In this study, the plasmonic behavior of silver nanoparticles encapsulated in diverse copolymer dielectric environments was investigated, focusing on the analysis of the emerging localized surface plasmon resonances (LSPRs) through both experimental and theoretical approaches. Specifically, two series of nanostructured silver ultrathin films were deposited via magnetron sputtering on heated Corning Glass substrates at 330 °C and 420 °C, respectively, resulting in the formation of self-assembled NPs of various sizes and distributions. Subsequently, three different polymeric layers were spin-coated on top of the silver NPs. Optical and structural characterization were carried out by means of UV–Vis spectroscopy and atomic force microscopy, respectively. Rigorous Coupled Wave Analysis (RCWA) was employed to study the LSPRs theoretically. The polymeric environment consistently induced a red shift as well as various alterations in the LSPR amplitude, suggesting the potential tunability of the system.

Keywords: self-assembly; silver nanoparticles; plasmonics; LSPR; copolymers; hybrid nanostructured films; RCWA

1. Introduction

In recent years, plasmonics has undergone remarkable development, attracting significant research interest centered on the unique optical properties of plasmonic NPs. These are metallic nanoparticles with sizes smaller than the wavelength of visible light that can be fabricated by a plethora of methods, including chemical synthesis [1,2], lithography [3], sputtering [4,5], laser ablation [6,7], green synthesis [8], and more [9–11], finding applications in various fields such as optoelectronics, catalysis, biological, and chemical sensing, photothermal therapy, and light harvesting [2,10,12–16].

Upon irradiation by electromagnetic waves, plasmonic nanoparticles' free electrons exhibit a collective oscillation at a resonant frequency, manifesting a phenomenon known as localized surface plasmon resonance (LSPR). This phenomenon can result in the intense absorption of light as well as the enhancement of the local electromagnetic field. LSPRs are important for numerous applications and have been exploited to enhance solar cell efficiency [12,13], fabricate highly sensitive biosensing devices for medical diagnostics and bioimaging [10,15], as well as improve catalytic [14] and optoelectronic performance [13].

Over the years, researchers have dedicated their efforts to integrating two or more elements into synthetic nanostructures, aiming to create multifunctional materials with enhanced capabilities. One notable approach involves combining plasmonic nanoparticles

with polymers, resulting in the development of plasmonic–polymer nanocomposites and hybrid plasmonic nanostructures [17–20]. The goal of this combination is to obtain novel materials and devices with enhanced functionality and responsiveness [21–23]. The synergistic effects of these hybrid nanostructured materials can be leveraged in functional systems, endowing them with remarkable optoelectronic, sensing, catalytic, and antibacterial properties, as well as improved light harvesting efficiency [17,18,24–28]. These attributes render these materials highly versatile and suitable for applications in diverse fields.

Functional polymer composites with embedded metal nanoparticles have been fabricated using numerous methods, including reduction of metal salts, plasma polymerization combined with metal deposition, co-evaporation of metals and organic components, and co-sputtering. Further details on the synthesis methods of such composites can be found in references [17,18,29].

Polymers are excellent candidates to be used as matrices or coatings due to their typically low cost, versatility, and ease of processing [17]. They also provide stability and biocompatibility of NPs in such nanostructured systems [25,30,31]. Furthermore, the refractive index of the polymers can substantially affect the LSPR features of these systems since the plasmonic properties of metallic nanoparticles are strongly influenced by their dielectric environment [2,9,32]. Therefore, the careful selection of constituent materials is crucial for shaping the optical properties and determining the features of these functional plasmonic polymer systems.

In this context, it is important to introduce copolymers, also known as heteropolymers, which constitute a class of polymers synthesized from two or more distinct monomeric species. Copolymers can display enhanced properties due to interactions between the monomer units, resulting in synergistic effects beyond individual monomers' capabilities. Block copolymers, a specific class of copolymers, consist of two or more chemically distinct polymer blocks that are covalently linked together, forming a larger and more complex macromolecule. Block copolymers can exhibit phase separation, resulting in the formation of periodic domains on the nm scale. These domains may adopt spherical, lamellar, or cylindrical geometries depending on molecular parameters such as the Flory–Huggins interaction parameter (χ), the degree of polymerization (N), and the volume fraction (f) of the blocks [33–37]. This remarkable property can be utilized in a plethora of applications, including nanopatterning, microelectronics, drug delivery, photovoltaics, and battery applications, as described in references [33–39] and references therein. Given their unique characteristics, we opted to use copolymers (including block copolymers) in our study. These polymeric materials are employed to coat silver nanoparticles, effectively modifying their dielectric environment and consequently altering their LSPR response [40].

Moreover, the choice of utilizing silver NPs in our study is grounded in silver's emergence as a leading noble metal in plasmonic applications, due to its minimal optical losses, stability in nanoparticle form, and strong LSRP absorption within the visible spectrum. In addition, its affordability compared to other noble metals makes silver an excellent choice for various plasmonic applications [41].

While polymer–plasmonic nanoparticle systems have been mostly explored for their functionality, it appears that there is less emphasis on the investigation of the fundamental optical properties of these materials. Our study investigates the LSPR properties of silver nanoparticles before and after coating them with various copolymers, both experimentally and theoretically. This investigation aims to provide valuable insights into the plasmonic behavior of the system and its potential tunability.

More specifically, silver NPs were grown via magnetron sputtering on heated glass substrates at 330 °C and 420 °C, respectively. Subsequently, they were covered with three different copolymers by means of spin coating. The copolymer-coated NPs showed systematic red shifts in the resonance position along with various LSPR amplitude alterations. Finally, we conducted rigorous coupled-wave analysis (RCWA) theoretical calculations. These calculations not only complemented the experimental results but also provided

deeper insights into the LSPRs of silver NPs within each polymeric environment. This approach offered a more comprehensive understanding of the observed phenomena.

2. Materials and Methods

2.1. Experimental Details

Two series of nanostructured ultrathin Ag films with nominal thicknesses ranging from 5 to 15 nm were deposited via direct-current (DC) magnetron sputtering on Corning glass at 330 °C and 420 °C. Under these deposition conditions, all films were directly self-assembled into NPs. Therefore, when referring to the nominal thickness of a nanostructured film, we refer to the thickness of a continuous Ag film that would form under the same deposition time at room temperature. In the DC magnetron sputtering process, a sputter-coater device (modified Balzers Union model SCD040, Oerlikon Balzers, Balzers, Liechtenstein) with a heated substrate holder was employed. By utilizing a dual-stage rotation pump, the base pressure of the chamber was maintained at 1.5×10^{-2} mbar. During deposition, argon was introduced into the chamber, increasing the total pressure to 5×10^{-2} mbar.

Subsequently, all nanostructured Ag films were coated with three different polymeric coatings by means of spin-coating. For the fabrication of the polymeric coatings (matrices), we used solid solutions of three different copolymers: polystyrene-block-polybutadiene-block-polystyrene (PS-b-PBD-b-PS), poly(styrene-co-methyl methacrylate) (PS-co-PMMA), and polystyrene-block-polyisoprene-block-polystyrene (PS-b-PI-b-PS), respectively. Each of the copolymers was dissolved into toluene, thus creating a 1.5% w/w solution. Specifically, 0.092 gr of PS-b-PBD-b-PS, 0.096 gr of PS-co-PMMA, and 0.065 gr of PS-b-PI-b-PS were dissolved in 6.143, 6.432, and 4.371 gr of toluene solution, respectively. The copolymers were deposited on the NPs by a spin-coating device (KW-4A, Chemat Scientific, Northridge, CA, USA).

The optical properties of both coated and uncoated films were investigated via ultraviolet–visible (UV–Vis) spectroscopy using the Perkin Elmer λ-35 spectrometer (PerkinElmer, Akron, OH, USA) operating at room temperature in the wavelength range of 200–1100 nm.

The surface morphology of the uncoated films was studied via atomic force microscopy (AFM). Film and polymer thickness determination was performed using atomic force microscopy (AFM) images showing the profile of a narrow scratch conducted intentionally on the film surface [40,41]. The thickness of polymer films deposited on a Corning glass substrate was measured at 54, 35, and 300 nm for PS-b-PBD-b-PS, PS-co-PMMA, and PS-b-PI-b-PS, respectively. The employed AFM device was a multimode microscope with a Nanoscope IIIa controller and a 120×120 µm^2 magnet-free scanner (Model AS-130VMF) developed by Digital Instruments (Chapel Hill, NC, USA) operating in the non-contact (tapping) mode [42].

2.2. Theoretical Model

The simulation model applied for the needs of the present article is the interpretation of the Rigorous Coupled-Wave Analysis (RCWA Method), a significant tool characterized for the accuracy of its results when it comes to the study of propagating electromagnetic waves into periodic matrices [43]. Figure 1 depicts the side and top views of the examined system with the Ag NPs placed on top of SiO$_2$ and surrounded by a different copolymer at a time. For net silver NPs, the dielectric environment was substituted with air. Ag NPs are depicted as cylinders or cubes because it is proven that these geometrical shapes consume less computational time and resources once simulated when applying RCWA [44,45]. A periodic array is also performed in order to balance the presence of one individual NP, which is non-evaluated due to the observed proximity of Ag NPs fabricated in situ along with the observed disorder structure probed by AFM.
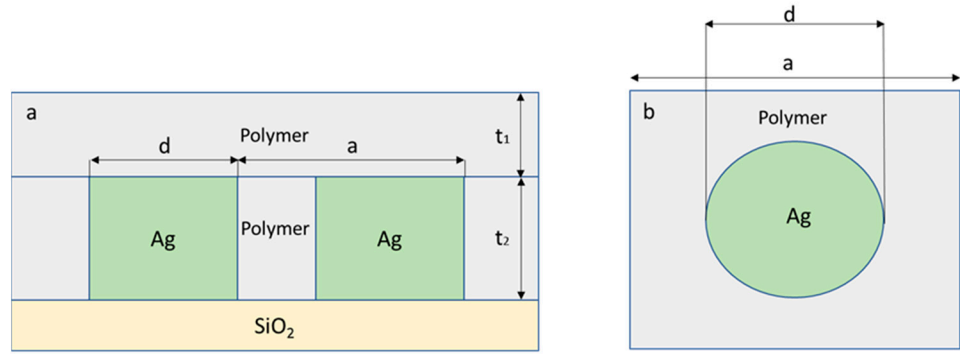
Figure 1. The modeled system composed of Ag NPs inside a polymeric environment ((**a**) side view, (**b**) top view). Geometric features of diameter (d) and lattice constant (a) are illustrated.

RCWA is also known for its advantages in terms of computational time because the investigated area is divided into layers in which the values of refractive indices are considered stable. Thus, the eigenvalues of the refractive indices are solved in the form of a matrix by applying Fourier expansions.

The relative permittivity for each layer is described as follows:

$$\varepsilon\left(x,y,z\right) = \varepsilon(x + \Lambda, y + \Lambda, z) = \sum_{p,q} \varepsilon_{pq}(z)e^{i(pK_x x + qK_y y)} \tag{1}$$

where Λ is the grating period, ε_{pq} is the Fourier component of grating permittivity, and K is the reciprocal lattice vectors defined as follows: $K_x = K_y = 2\pi/\Lambda$, where Λ is the lattice constant and $i = (-1)^{1/2}$.

The mathematical formula of the electric field in Region I, the incoming region, which is the air region above the structure, is the following:

$$E_I = e^{-i(k_{xi}x + k_{yi}y + k_{zi}z)} + \sum_{nm} R_{nm}e^{-i(k_{xn}x + k_{ym}y + k_{znmi}z)} \tag{2}$$

where $k_{xn} = k_{x0} + nK_x$, $k_{yn} = k_{y0} + mK_y$, $k_{znmi} = \sqrt{(k^2\varepsilon_i - k^2_{xn} - k^2_{ym})}$, k_{x0} and k_{y0} are the x and y components of the incident plane wave, and $k = 2\pi/\lambda$, R_{nm} is the n, m order backward diffracted wave.

Regarding Region II, which includes the regions between I and III (in practice, we divide it into two t_1 and t_2 in Figure 1), the mathematical formula of the electric field for each layer is the following:

$$E_{II} = \sum_{nm} S_{nm}(z)e^{-i(k_{xn}x + k_{ym}y + k_{znmi}z)} \tag{3}$$

where $S_{nm}(z)$ are the space harmonic field amplitudes, and as for Region III, the outcoming region, which is the SiO_2 region (assumed semi-infinite), the electric field is described by the next formula:

$$E_{III} = \sum_{nm} T_{nm}e^{-i(k_{xn}x + k_{ym}y + k_{znmo}(z-d))} \tag{4}$$

where $k_{znmo} = \sqrt{(k^2_{\varepsilon o} - k^2_{xn} - k^2_{ym})}$; T_{nm} is the n, m order forward diffracted wave. This analysis also applies to the magnetic field.

Keeping N and M harmonics in Equations (2)–(4), and from the continuity of the tangential electric and magnetic fields at the boundaries $z = 0$ and $z = d$, a 4NM system of equations emerges, leading to the solution of Rnm and Tnm values [40].

3. Results

3.1. Experimental Results

3.1.1. Microstructure, UV–Vis Spectra, and LSPR Analysis of Uncoated Nanoparticles

AFM images in Figures 2a–c and 3a–c illustrate self-assembled silver nanoparticles in all examined films, accompanied by their respective nanoparticle diameter distributions (Figures 2d–f and 3d–f). Dense NP distributions with several agglomerates can be observed in all cases. Films with nominal thicknesses of 5 and 10 nm showed single nanoparticle distributions at both deposition temperatures, whereas the two thicker (15 nm) films displayed bimodal distributions. This is further supported by the presence of secondary absorbance peaks around 3.6 eV. The diameters of the NPs depended on the nominal thickness of the films, and detailed mean nanoparticle diameter values are presented in Table 1.

Larger NPs were observed with increasing film thickness at both deposition temperatures. This trend is further supported by the corresponding nanoparticle diameter distributions shown in Figures 2d–f and 3d–f. The fitting was performed using the logarithmic-normal distribution function. Furthermore, it can be observed that the 10 nm films exhibited almost identical NP distributions at both substrate temperatures, which explains their nearly identical absorbance curves. In the case of the 5 nm films, higher substrate temperatures led to the formation of larger NPs, as observed in the 15 nm films. In the latter case, the mean NP diameters of the bimodal distribution were smaller at 420 °C. However, the number of small NPs (< 60 nm) decreased, while there was a significant increase in the number of larger NPs. The presence of more large NPs could justify the substantial enhancement of LSPR amplitude compared to 330 °C.

5 nm   **10 nm**   **15 nm**

(**a**)   (**b**)   (**c**)

(**d**)   (**e**)   (**f**)

Figure 2. (**a**–**c**) AFM images of the nanostructured films deposited at 330 °C along with their respective nanoparticle diameter distributions (**d**–**f**). The nominal thickness of each film is indicated above.
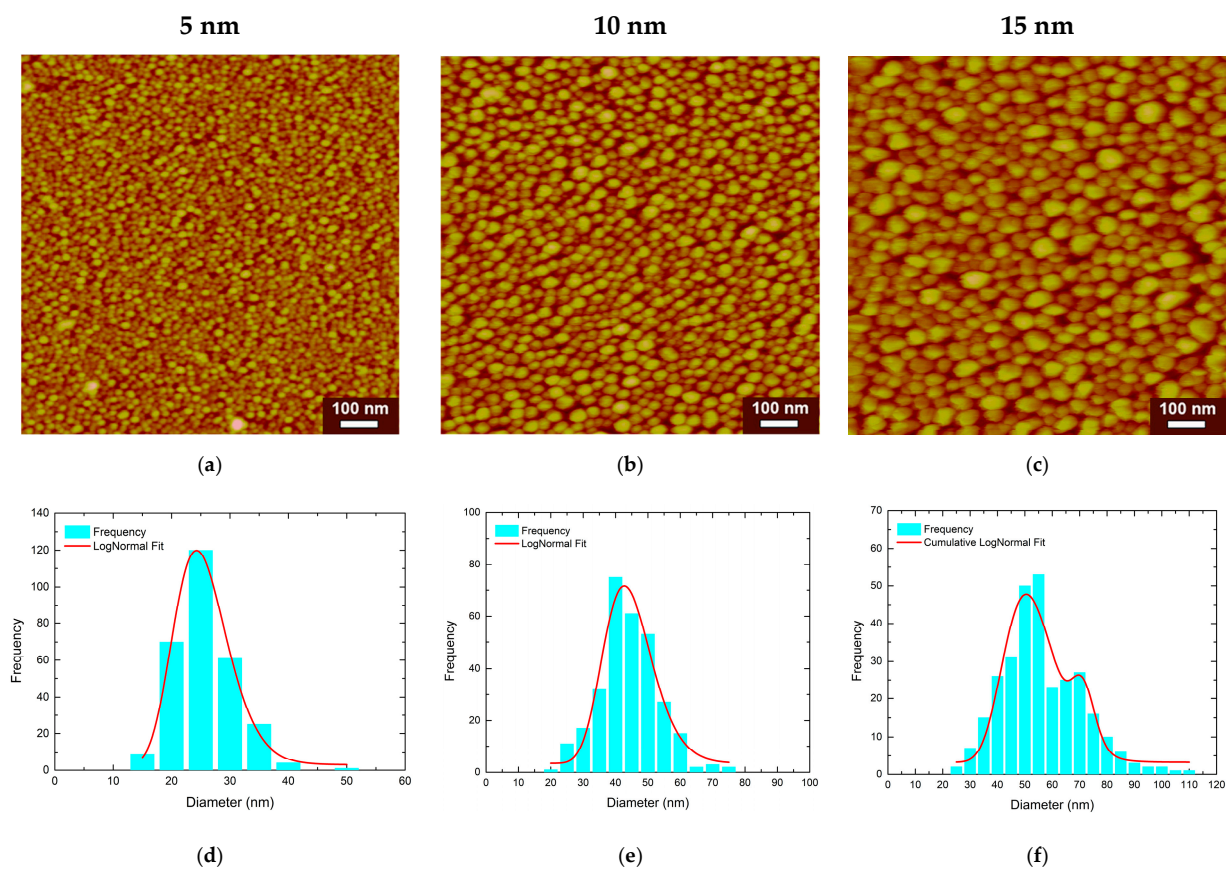
(a) (b) (c)

(d) (e) (f)

(g) (h)

Figure 3. (**a**–**c**) AFM images of the nanostructured films deposited at 420 °C along with their respective nanoparticle diameter distributions (**d*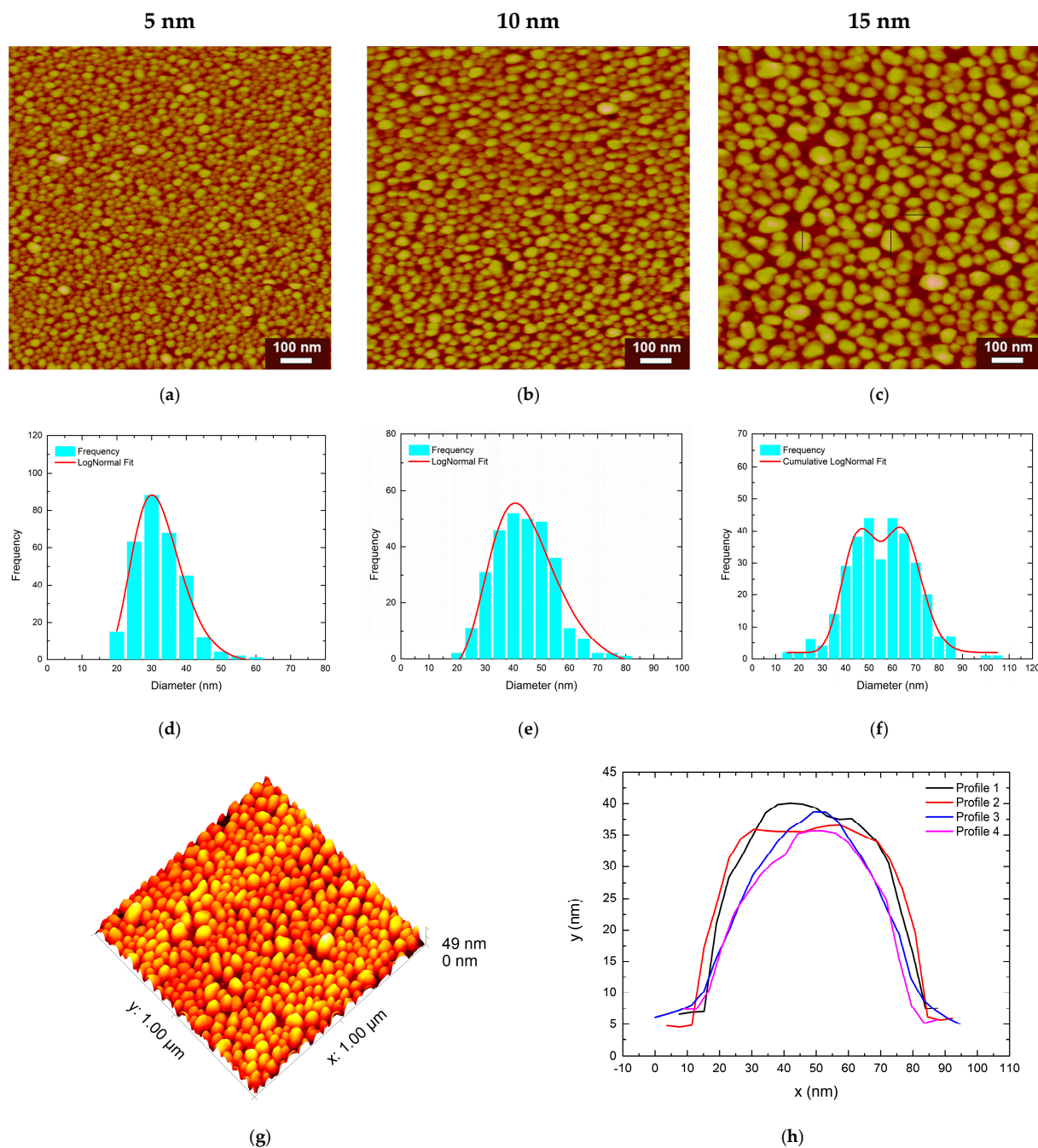*–**f**). The nominal thickness of each film is indicated above. (**g**) 3D version of AFM (**c**) and (**h**) NP line profiles of (**c**).

Table 1. Mean NP diameter values as a function of deposition temperature and nominal film thickness for all distributions illustrated in Figure 2.

Deposition Temperature	Mean NP Diameter			
	5 nm	10 nm	15 nm	
330 °C	25 nm	44 nm	52 nm	72 nm
420 °C	32 nm	44 nm	48 nm	66 nm

Figure 4 illustrates the UV–Vis spectra for two series of three nanostructured ultrathin Ag films with nominal thicknesses of 5, 10, and 15 nm. Both series were deposited on Corning glass, with the first series being deposited at 330 °C and the second series at 420 °C, respectively.
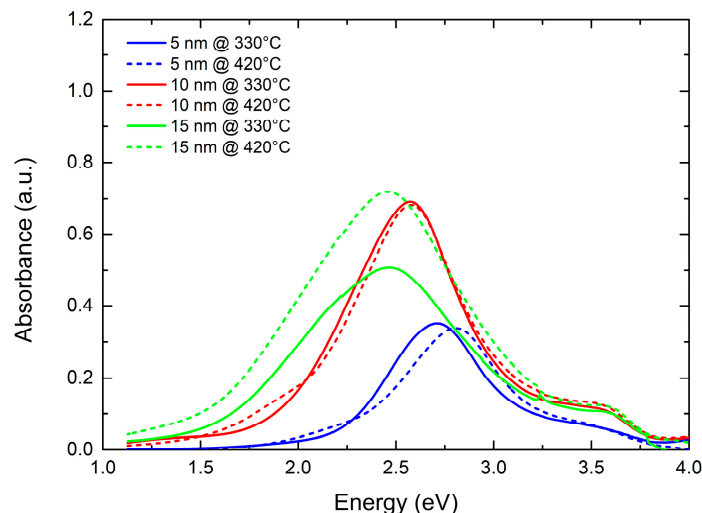

Figure 4. UV–Vis spectra for the two series of nanostructured ultrathin Ag films with nominal thicknesses of 5, 10, and 15 nm. Solid lines represent absorbance curves for films deposited at 330 °C, and dashed lines correspond to those deposited at 420 °C.

LSPRs were obtained in all cases, located between 2.46 and 2.81 eV, with the deposition temperature having a minimal effect on the LSPR position. Only the thinner (5 nm) film exhibited a slight blue shift with increased substrate temperature. On the contrary, regarding the LSPR amplitude, while it remained almost identical for the two thinner films (5 and 10 nm) at both deposition temperatures, the 15 nm film grown at 420 °C exhibited a significantly larger amplitude compared to the film of the same thickness deposited at 330 °C. The variations in full width at half-maximum (FWHM) for the two different substrate temperatures were negligible, with the 5 nm films exhibiting the lowest FWHM values (sharper LSPRs) and the 15 nm films the largest (broader LSPRs).

3.1.2. UV–Vis Spectra and LSPR Analysis of Polymer-Coated Nanoparticles

In Figure 5a–f, UV–Vis spectra of the previously discussed nanostructured films are presented after their coating with various polymers. The absorbance curve of the uncoated films is also included for a clearer comparison.

Notably, a consistent red shift in the LPSR position is observed across all coated films. This could be attributed to the larger dielectric constant of the polymeric coatings compared to that of air.

Regarding the LPSR amplitude, alterations were observed after coating with each copolymer, yet without an unambiguous dependence on a specific parameter. Furthermore, the following observations were made: For the 5 nm films, the PS-b-PI-b-PS coating substantially decreased the LPSR amplitude, whereas the PS-co-PMMA induced a slight increase. Moreover, the third copolymer, PS-b-PBD-b-PS, resulted in an almost identical absorbance curve to the PS-co-PMMA-coated film for the film deposited at 330 °C. However, the PS-b-PBD-b-PS coating decreased the LSPR amplitude for the 5 nm film deposited at 420 °C.
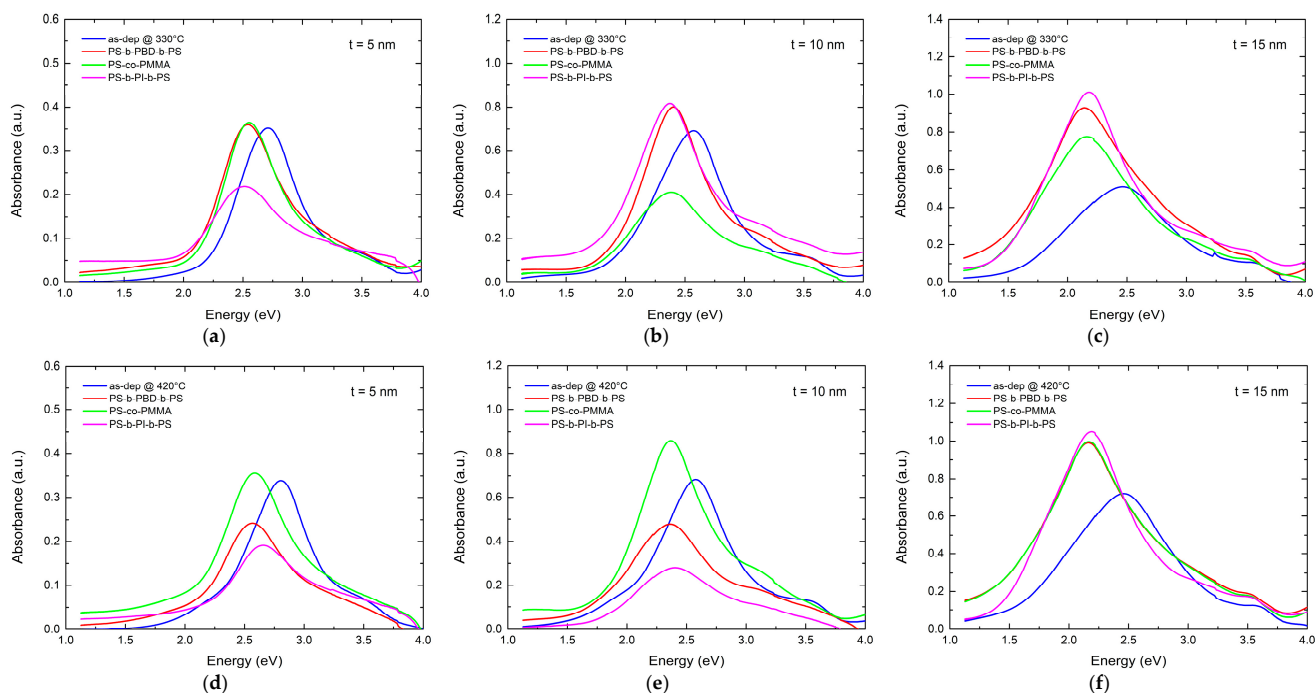
Figure 5. UV–Vis spectra for the two series of nanostructured ultrathin Ag films with thicknesses of 5, 10, and 15 nm after coating with PS-b-PBD-b-PS, PS-co-PMMA, and PS-b-PI-b-PS copolymers. (**a–c**) shows UV–Vis spectra for the first series, deposited at 330 °C, and (**d–f**) for the second series, deposited at 420 °C.

In the case of 10 nm films, the polymeric coatings induced inconsistent changes in the LSPR amplitude. Despite observing similar absorbance curves and NP distributions for both 10 nm films, no consistent pattern in the alterations of resonance amplitude was identified. On the contrary, an inverse variation of the amplitude of the two films was observed for each copolymer used.

Lastly, in the 15 nm films, a consistent pattern could be observed, with all the polymeric coatings resulting in increased resonance amplitude. Specifically, PS-b-PI-b-PS induced the largest enhancement, followed by PS-b-PBD-b-PS. PS-co-PMMA had a similar effect to PS-b-PBD-b-PS for the film deposited at 420 °C, resulting in almost indistinguishable absorbance curves. Conversely, PS-co-PMMA had a smaller impact on the enhancement of LSPR amplitude for the film deposited at 330 °C.

Interestingly, in the latter case (15 nm films), the FWHM was decreased substantially after applying the polymeric coatings, resulting in sharper LSPRs. For the rest of the specimens, FWHM varied, exhibiting both increases and decreases.

The polymeric coatings have had a greater effect on larger NPs, particularly noticeable in films with a nominal thickness of 15 nm, which appeared to be more sensitive to the polymeric coatings in terms of LSPR amplitude and FWHM. Additionally, as previously mentioned, the LSPR position shifted towards lower energies (red shift) in all cases. However, as shown in Figure 6a,b, this effect was more pronounced for the 15 nm films. Next, Figure 6c–f illustrate the variations of LPSR amplitude and FWHM as a function of nominal film thickness for the two deposition temperatures.
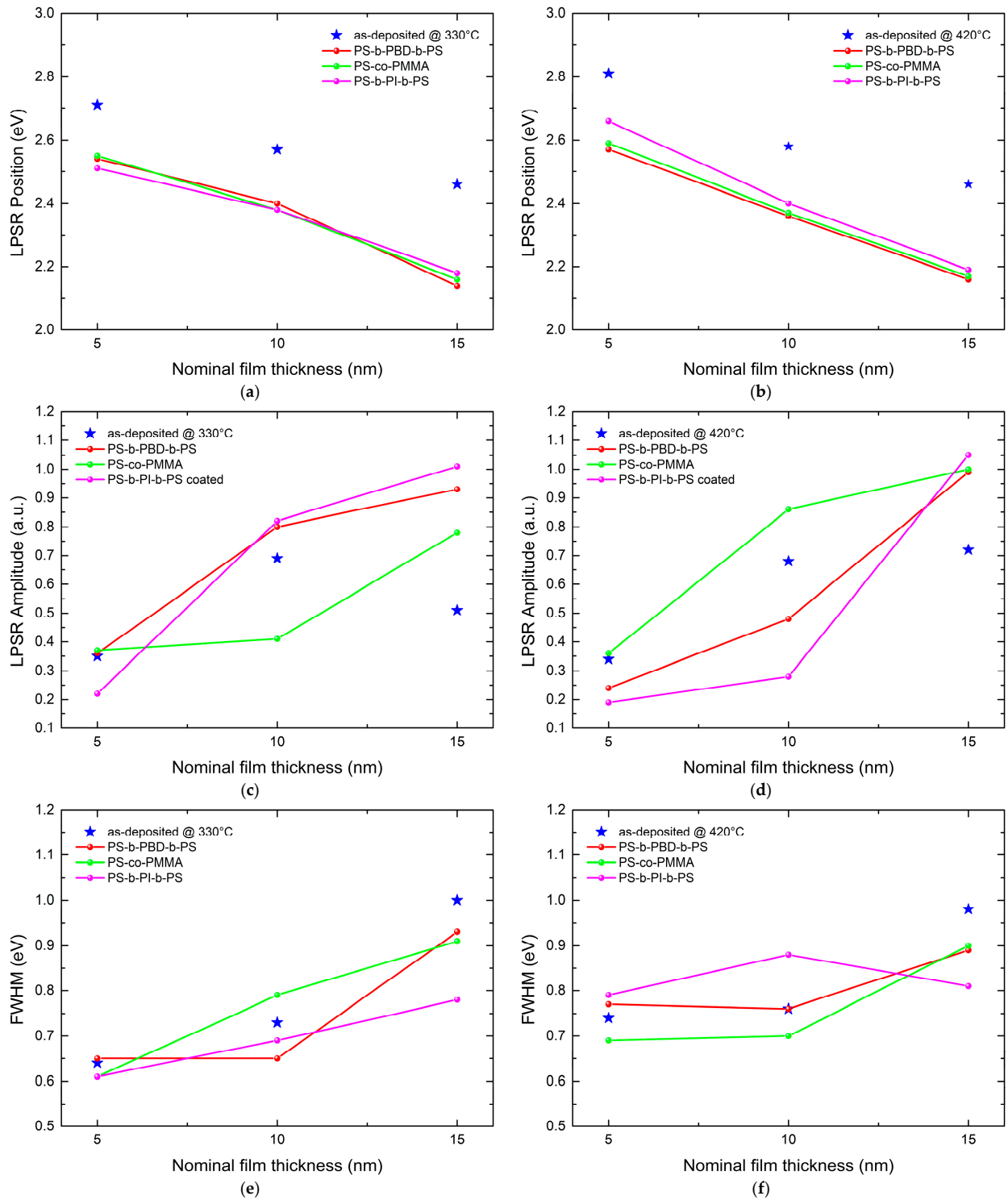
Figure 6. A visual representation of the polymeric coatings' influence on the LSPR characteristics of self-assembled NPs as a function of nominal film thickness for both deposition temperatures. (**a**,**b**) correspond to the alterations of LSPR position; (**c**,**d**) the alterations of LSPR amplitude; and (**e**,**f**) the alterations of the LSPR FWHM.

3.2. Theoretical Results

Here, we discuss the theoretical results generated after the implementation of the simulation method RCWA, thoroughly presented in Section 2.2. To ensure reliable conclusions, the nature of polymeric coatings is the same as during the experimental phase in order to straightforwardly compare the produced results. Three different copolymers were alternated, with the numeric values of their refractive indices being very close. In particular, the refractive index for PS-co-PMMA was 1.491, 1.521 for PS-b-PI-b-PS, and 1.539 for PS-b-PBD-b-PS [46].

We have to notice that, as we can see in the AFM images of Figures 2a–c and 3a–c, the shape and the diameter of the metallic nanoparticles are highly disordered. Moreover, the line profiles of the particles (Figure 3g,h) show that their shape is distorted and partially flattened hemispheres. It is computationally impossible to simulate the exact structure since that will involve a huge supercell. For that reason, we used cylindrical-shaped metallic nanoparticles with an average diameter like the measured one. Indeed, it is much faster to do the calculations with cylindrical-shaped metallic nanoparticles, since this is the advantage of the RCWA method. Additionally, previous studies, see for example Ref. [47], showed good agreement between calculations and measurements.

In Figure 7, we present calculated absorbance spectra for uncoated and coated Ag NPs. The diameter (d) of the NPs was selected to be 30, 45, and 60 nm, as these values are similar to the average ones of the experimentally grown NPs presented in Table 1. The periodicity (a) was selected to be equal to $3/2 \times$ d. In Ref. [45], we have shown that any selection of a between $3/2 \times$ d and $3 \times$ d does not change the position of the LSPR. The parameter t_1 was selected to be 35 nm [40]. In Figure 7a, we present the uncoated and coated PMMA Ag NPs for $t_2 = d/3$, i.e., for slightly flattened hemispheres, while in Figure 7b the same is true for $t_2 = d/2$, i.e., for perfect hemispheres. In Figure 7c,d, all parameters are the same as in Figure 7a, but we use different polymeric coatings. We have to note the following: The LSPRs of the coated Ag NPs always show a red shift with respect to the uncoated ones, and they are slightly larger. This is due to the increase in the refractive index of the dielectric medium by switching from air to polymer. This red shift is very similar to one of the LSPRs in the experimental spectra in Figure 5b. The shapes of the LSPRs in Figure 7a are more similar to the experimental ones, unlike the ones in Figure 7b. That is, by increasing the height of the NPs, the second (higher) LSPR resonance becomes much more pronounced and can even exceed the height of the first (main) one. Moreover, all spectra in Figure 7b are blue-shifted compared to the ones in Figure 7a,c. The width of the calculated LSPRs is practically the same for all values of d. However, the experimental ones for the larger values of d (15 nm films) are quite broad. This is probably due to the fact that the size distribution of d in that case is quite large (bimodal growth). Finally, a comparison of the LSPRs for coated Ag NPs with different polymers (Figure 7a,c,d) shows that they are very similar since the refractive index of the various polymers varies only by a few percent.

In Figure 8, we present the modifications of the LSPRs with polymer-coating thickness, leaving all parameters as in Figure 7c,d and setting the polymeric coating equal to the experimental one [40]. One may hardly see a difference in the LSPR position. However, the intensity of the LSPRs seems to increase with increasing polymer thickness.
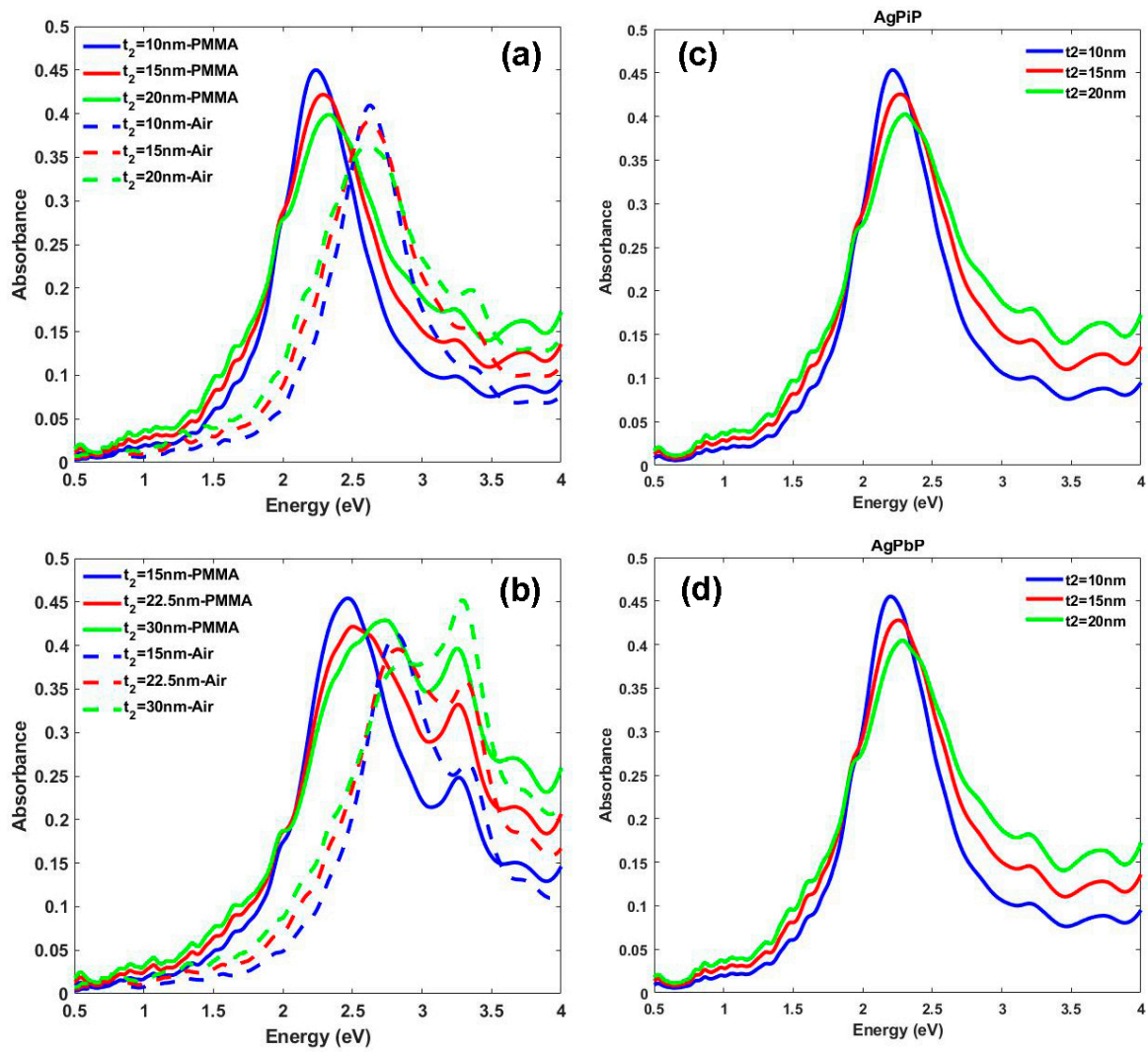
Figure 7. Size-dependent LSPRs in polymeric-coated Ag NPs ((**a**) PS-co-PMMA, (**b**) as in (**a**), however, t_2 increases from d/3 to d/2, (**c**) PS-b-PI-b-PS, and (**d**) PS-b-PBD-b-PS).
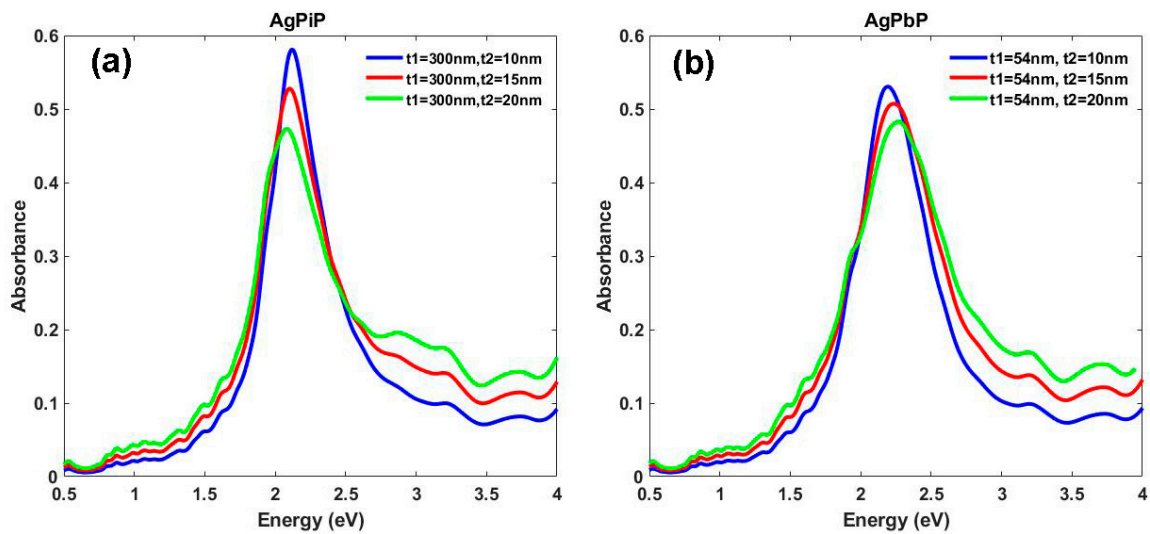

Figure 8. LSPRs calculated for different values of the thickness of polymer-coated Ag NPs. In (**a**), the polymer coating is PS-b-PI-b-PS, and in (**b**), it is PS-b-PBD-b-PS.

4. Discussion

The plasmonic behavior of the silver NP-copolymer system was investigated through both experimental and theoretical approaches.

More specifically, in the experimental part, initially, the deposition of two series of nanostructured ultrathin Ag films on heated substrates resulted in the formation of self-assembled silver NPs on corning glass substrates. The reason that we directly have the formation of self-assembled nanoparticles is the following: Silver does not wet glass easily due to the large difference in their surface energies: 1.25 J/m^2 for Ag [48], and only 0.3 J/m^2 for glass [49]. By increasing the temperature of the system, we drive it closer to the thermodynamic equilibrium state, which is island growth [50]. The nominal film thickness was 5, 10, and 15 nm for each series, leading to single NP distributions for the 5 and 10 nm thick nanostructured films and bimodal NP distributions for the thicker 15 nm films. The mean NP diameter values varied from 25 nm to 44 nm for the monomodal distributions of 5 and 10 nm films, respectively, while the peaks of the bimodal distributions had values of 52 nm and 72 nm for a deposition temperature of 330 °C. For 420 °C, the mean NP values were 48 nm and 66 nm. All specimens exhibited typical LSPRs for Ag NPs [47]. For the thicker (15 nm) films, a secondary LSPR could be detected around 3.6 eV due to their bimodal distribution. These secondary resonances might be the result of multiple scattering within the film's nanostructure due to the presence of very small NPs [47]. As was expected, increasing film thickness resulted in larger NPs for both deposition temperatures. Notably, as shown in Figure 4, elevated deposition temperature had a bigger impact on the LSPR position of thinner films (5 nm) and the LSPR amplitude of thicker films (15 nm). Interestingly, the 10 nm films had almost indistinguishable LSPRs owing to their similar NP distributions.

After spin coating the copolymers PS-b-PBD-b-PS, PS-co-PMMA, and PS-b-PI-b-PS onto the nanostructured films, UV–Vis spectra revealed the following observations: A consistent red shift in the LPSR position was observed across all coated films (refer to Figures 5a–f and 6a,b). This could be attributed to the larger value of the dielectric constant of the polymeric coatings (~1.5) compared to that of air. This consistent red shift has also been observed in Au and Ag NPs in NiO [44,45] and ZnO [41] dielectric environments, due to their relatively large dielectric constants. Additionally, the same trend was also observed when investigating the impact of similar polymeric coatings on the plasmonic behavior of Au NPs [40].

Regarding LSPR amplitude, the application of copolymer coatings induced alterations without exhibiting a clear dependence on any specific parameter for the 5 and 10 nm thick films. However, the LSPR amplitude consistently increased for all copolymer coatings in the thicker (15 nm) films. Additionally, after coating, the latter films exhibited narrower resonances, i.e., smaller FWHM, while the variations in FWHM in the thinner films were not consistent. A possible explanation for these observations could be the following: The polymeric coatings might have contributed more significantly and consistently to the enhancement of the LSPR amplitude of sparser NP distribution (15 nm films) due to the larger interparticle distance. Specifically, since there was more space between the NPs, the polymeric coating could be deposited uniformly and modify the properties of individual NPs uniformly, leading to consistent increases in the LSPR amplitude. On the contrary, in very dense NP distributions (5 and 10 nm films), the contact of the polymeric coating with the NP surface might not be as uniform, thus leading to complex interactions between neighboring NPs and finally mixed effects on the LPSR amplitude. As for the FWHM decrease, the polymeric coatings might have contributed to weaker interparticle coupling in the sparser NP distributions, resulting in narrower resonances. These observations show that there is room for potential tuning of the LSPRs in the Ag NP copolymer hybrid films; however, deeper investigation is required to precisely tailor their plasmonic characteristics.

In our theoretical analysis, the LSPR behavior was investigated for varying NP diameter values, periodicity, and NP height, with or without the polymeric coatings (Figure 7a–d). Given the flattened hemispherical morphology of the experimentally grown NPs, calcula-

tions were conducted using cylindrical metallic nanoparticles with a comparable average diameter in order to better mimic their observed structure. The calculated LSPRs of these cylindrical metallic nanoparticles shown in Figure 7a,c,d exhibited absorption patterns closer to those observed experimentally, thus validating our approach in these calculations. Furthermore, it was observed that the calculated LSPRs for all coated NPs were very similar, due to the small differences in the refractive indexes of the copolymers employed. Simulations comparing the LPSRs with and without the polymeric coatings consistently reproduced a red shift in all studied cases, in complete agreement with the experimental results. The red shift was accompanied by an increase in the LPSR amplitude for the calculated results. These observations can be attributed to the larger refractive index of the copolymers compared to that of air. However, as discussed above, experimental results did not display similar consistency regarding LSPR amplitude behavior. Moreover, for coated NPs, we investigated the copolymer-layer thickness influence on the LPSRs (Figures 7c,d and 8a,b). The LSPR position showed negligible changes; however, the LSPR amplitude seemed to increase with increasing copolymer thickness. In contrast, experimental results did not reveal a similar pattern. Lastly, the calculated width of LSPRs was practically the same for all diameter values, not completely aligning with the experimental results, which showed broader LSPRs for larger diameter values.

Overall, an exact reproduction of the LSPR behavior was not expected, as our theoretical calculations investigated a range of NP diameters to identify general trends. Since our aim was not to precisely predict the experimental absorbance, discrepancies between theoretical and experimental results were anticipated. Additionally, it is very difficult to fully predict the LSPR behavior theoretically since the fabricated NPs have a disordered structure and their shape is not perfectly spherical across the substrate's surface. This is due to the fact that we utilized self-assembly as a growth method. While practical and cost-effective, it does not guarantee complete control over the fabricated NP arrays, unlike the precise but costly lithographic techniques.

Ultimately, this study showed that the LSPR features of silver NPs could be tuned considerably after coating with various copolymers. These findings indicate the potential of these hybrid nanostructured films as valuable components in applications such as biological or chemical sensing that could exploit the synergistic properties of plasmonic NPs and polymeric coatings.

5. Conclusions

This study demonstrated experimental and theoretical analyses of the LSPR characteristics of self-assembled Ag NPs coated with various copolymers. The polymeric coatings induced systematic red shifts in the plasmonic resonances, a trend also observed theoretically. Additionally, LSPR amplitude was enhanced in our theoretical results and some experimental cases; however, this enhancement was not consistent across all experimental results. The resonance width also showed discrepancies between experimental and theoretical results for larger NPs, which can be attributed to their diameter distribution. The utilization of copolymers showed promise in terms of tunability potential, and such hybrid systems could be useful for sensing or other applications that could leverage polymeric-coated or encapsulated plasmonic NPs.

Author Contributions: Conceptualization, S.G.; methodology, A.S. and P.P.; software, M.T.; validation, M.S.; formal analysis, D.G.; investigation, V.K. and D.N.; resources, P.P. and M.S.; data curation, A.S., D.N. and M.T.; writing—original draft preparation, D.N. and M.T.; writing—review and editing M.S. and P.P.; visualization, S.G.; supervision, S.G.; project administration, P.P. and M.S. All authors have read and agreed to the published version of the manuscript.

Institutional Review Board Statement: Not applicable.

Informed Consent Statement: Not applicable.

Data Availability Statement: The data are contained within the article.

Conflicts of Interest: The authors declare no conflicts of interest.

References

1. Lu, X.; Rycenga, M.; Skrabalak, S.E.; Wiley, B.; Xia, Y. Chemical Synthesis of Novel Plasmonic Nanoparticles. *Annu. Rev. Phys. Chem.* **2009**, *60*, 167–192. [CrossRef]
2. Yang, P.; Zheng, J.; Xu, Y.; Zhang, Q.; Jiang, L. Colloidal Synthesis and Applications of Plasmonic Metal Nanoparticles. *Adv. Mater.* **2016**, *28*, 10508–10517. [CrossRef]
3. Gisbert Quilis, N.; Lequeux, M.; Venugopalan, P.; Khan, I.; Knoll, W.; Boujday, S.; Lamy De La Chapelle, M.; Dostalek, J. Tunable Laser Interference Lithography Preparation of Plasmonic Nanoparticle Arrays Tailored for SERS. *Nanoscale* **2018**, *10*, 10268–10276. [CrossRef] [PubMed]
4. Asanithi, P.; Chaiyakun, S.; Limsuwan, P. Growth of Silver Nanoparticles by DC Magnetron Sputtering. *J. Nanomater.* **2012**, *2012*, 79. [CrossRef]
5. Nguyen, M.T.; Zhang, H.; Deng, L.; Tokunaga, T.; Yonezawa, T. Au/Cu Bimetallic Nanoparticles via Double-Target Sputtering onto a Liquid Polymer. *Langmuir* **2017**, *33*, 12389–12397. [CrossRef] [PubMed]
6. Piotto, V.; Litti, L.; Meneghetti, M. Synthesis and Shape Manipulation of Anisotropic Gold Nanoparticles by Laser Ablation in Solution. *J. Phys. Chem. C* **2020**, *124*, 4820–4826. [CrossRef]
7. Rafique, M.; Rafique, M.S.; Kalsoom, U.; Afzal, A.; Butt, S.H.; Usman, A. Laser Ablation Synthesis of Silver Nanoparticles in Water and Dependence on Laser Nature. *Opt. Quant. Electron.* **2019**, *51*, 179. [CrossRef]
8. Aziz, S.B.; Hussein, G.; Brza, M.A.; J. Mohammed, S.; T. Abdulwahid, R.; Raza Saeed, S.; Hassanzadeh, A. Fabrication of Interconnected Plasmonic Spherical Silver Nanoparticles with Enhanced Localized Surface Plasmon Resonance (LSPR) Peaks Using Quince Leaf Extract Solution. *Nanomaterials* **2019**, *9*, 1557. [CrossRef] [PubMed]
9. Hutter, E.; Fendler, J.H. Exploitation of Localized Surface Plasmon Resonance. *Adv. Mater.* **2004**, *16*, 1685–1706. [CrossRef]
10. Demishkevich, E.; Zyubin, A.; Seteikin, A.; Samusev, I.; Park, I.; Hwangbo, C.K.; Choi, E.H.; Lee, G.J. Synthesis Methods and Optical Sensing Applications of Plasmonic Metal Nanoparticles Made from Rhodium, Platinum, Gold, or Silver. *Materials* **2023**, *16*, 3342. [CrossRef]
11. Nguyen, N.P.U.; Dang, N.T.; Doan, L.; Nguyen, T.T.H. Synthesis of Silver Nanoparticles: From Conventional to 'Modern' Methods—A Review. *Processes* **2023**, *11*, 2617. [CrossRef]
12. Atwater, H.A.; Polman, A. Plasmonics for Improved Photovoltaic Devices. *Nat. Mater* **2010**, *9*, 205–213. [CrossRef]
13. Liang, Z.; Sun, J.; Jiang, Y.; Jiang, L.; Chen, X. Plasmonic Enhanced Optoelectronic Devices. *Plasmonics* **2014**, *9*, 859–866. [CrossRef]
14. Li, S.; Miao, P.; Zhang, Y.; Wu, J.; Zhang, B.; Du, Y.; Han, X.; Sun, J.; Xu, P. Recent Advances in Plasmonic Nanostructures for Enhanced Photocatalysis and Electrocatalysis. *Adv. Mater.* **2021**, *33*, 2000086. [CrossRef]
15. Loiseau, A.; Asila, V.; Boitel-Aullen, G.; Lam, M.; Salmain, M.; Boujday, S. Silver-Based Plasmonic Nanoparticles for and Their Use in Biosensing. *Biosensors* **2019**, *9*, 78. [CrossRef] [PubMed]
16. Bastianini, F.; Hidalgo, A.I.C.; Hook, D.Z.; Smith, J.A.; Cumming, D.; Dunbar, A. Using Ag Nanoparticles in the Electron Transport Layer of Perovskite Solar Cells to Improve Efficiency. *Sol. Energy* **2024**, *268*, 112318. [CrossRef]
17. Faupel, F.; Zaporojtchenko, V.; Strunskus, T.; Elbahri, M. Metal-Polymer Nanocomposites for Functional Applications. *Adv. Eng. Mater.* **2010**, *12*, 1177–1190. [CrossRef]
18. Pastoriza-Santos, I.; Kinnear, C.; Pérez-Juste, J.; Mulvaney, P.; Liz-Marzán, L.M. Plasmonic Polymer Nanocomposites. *Nat. Rev. Mater.* **2018**, *3*, 375–391. [CrossRef]
19. Prakash, J.; Pivin, J.C.; Swart, H.C. Noble Metal Nanoparticles Embedding into Polymeric Materials: From Fundamentals to Applications. *Adv. Colloid Interface Sci.* **2015**, *226*, 187–202. [CrossRef]
20. Tokarev, I.; Minko, S. Tunable Plasmonic Nanostructures from Noble Metal Nanoparticles and Stimuli-Responsive Polymers. *Soft Matter* **2012**, *8*, 5980. [CrossRef]
21. Komshöft, T.; Bovone, G.; Bernhard, S.; Tibbitt, M.W. Polymer Functionalization of Inorganic Nanoparticles for Biomedical Applications. *Curr. Opin. Chem. Eng.* **2022**, *37*, 100849. [CrossRef]
22. Maleeva, K.; Dadadzhanov, D.; Palekhova, A.; Kaliya, I.; Tkach, A.; Baranov, A.; Bogdanov, K. SERS Substrates Based on Polymer-Protected Self-Assembled Plasmonic Films with Gold Nanoparticles as Enhancing Element of a Microfluidic Sensor. *Opt. Mater.* **2023**, *146*, 114581. [CrossRef]
23. Eddin, F.B.K.; Fen, Y.W.; Liew, J.Y.C.; Daniyal, W.M.E.M.M. Plasmonic Refractive Index Sensor Enhanced with Chitosan/Au Bilayer Thin Film for Dopamine Detection. *Biosensors* **2022**, *12*, 1124. [CrossRef]
24. Qian, C.; Guo, Q.; Xu, M.; Yuan, Y.; Yao, J. Improving the SERS Detection Sensitivity of Aromatic Molecules by a PDMS-Coated Au Nanoparticle Monolayer Film. *RSC Adv.* **2015**, *5*, 53306–53312. [CrossRef]

25. Potara, M.; Focsan, M.; Craciun, A.-M.; Botiz, I.; Astilean, S. Polymer-Coated Plasmonic Nanoparticles for Environmental Remediation: Synthesis, Functionalization, and Properties. In *New Polymer Nanocomposites for Environmental Remediation*; Elsevier: Amsterdam, The Netherlands, 2018; pp. 361–387. ISBN 978-0-12-811033-1.

26. Burko, A.; Zavatski, S.; Baturova, A.; Kholiboeva, M.; Kozina, J.; Kravtsunova, K.; Popov, V.; Gudok, A.; Dubkov, S.; Khartov, S.; et al. Polymer Membrane Modified with Photocatalytic and Plasmonic Nanoparticles for Self-Cleaning Filters. *Polymers* **2023**, *15*, 726. [CrossRef] [PubMed]

27. Alanazi, A.T.; Rice, J.H. Hybrid Composite Based on Conducting Polymers and Plasmonic Nanomaterials Applied to Catalysis and Sensing. *Mater. Res. Express* **2022**, *9*, 075002. [CrossRef]

28. Nugroho, F.A.A.; Darmadi, I.; Cusinato, L.; Susarrey-Arce, A.; Schreuders, H.; Bannenberg, L.J.; Da Silva Fanta, A.B.; Kadkhodazadeh, S.; Wagner, J.B.; Antosiewicz, T.J.; et al. Metal–Polymer Hybrid Nanomaterials for Plasmonic Ultrafast Hydrogen Detection. *Nat. Mater.* **2019**, *18*, 489–495. [CrossRef] [PubMed]

29. Pham, Q.T.; Ngo, G.L.; Nguyen, X.A.; Nguyen, C.T.; Ledoux-Rak, I.; Lai, N.D. Direct Synthesis of Gold Nanoparticles in Polymer Matrix. *Polymers* **2022**, *15*, 16. [CrossRef]

30. Scarabelli, L.; Schumacher, M.; Jimenez De Aberasturi, D.; Merkl, J.; Henriksen-Lacey, M.; Milagres De Oliveira, T.; Janschel, M.; Schmidtke, C.; Bals, S.; Weller, H.; et al. Encapsulation of Noble Metal Nanoparticles through Seeded Emulsion Polymerization as Highly Stable Plasmonic Systems. *Adv. Funct. Mater.* **2019**, *29*, 1809071. [CrossRef]

31. Kato, R.; Uesugi, M.; Komatsu, Y.; Okamoto, F.; Tanaka, T.; Kitawaki, F.; Yano, T. Highly Stable Polymer Coating on Silver Nanoparticles for Efficient Plasmonic Enhancement of Fluorescence. *ACS Omega* **2022**, *7*, 4286–4292. [CrossRef]

32. Kelly, K.L.; Coronado, E.; Zhao, L.L.; Schatz, G.C. The Optical Properties of Metal Nanoparticles: The Influence of Size, Shape, and Dielectric Environment. *J. Phys. Chem. B* **2003**, *107*, 668–677. [CrossRef]

33. Fasolka, M.J.; Mayes, A.M. Block Copolymer Thin Films: Physics and Applications. *Annu. Rev. Mater. Res.* **2001**, *31*, 323–355. [CrossRef]

34. Kim, H.-C.; Park, S.-M.; Hinsberg, W.D. Block Copolymer Based Nanostructures: Materials, Processes, and Applications to Electronics. *Chem. Rev.* **2010**, *110*, 146–177. [CrossRef] [PubMed]

35. Feng, H.; Lu, X.; Wang, W.; Kang, N.-G.; Mays, J. Block Copolymers: Synthesis, Self-Assembly, and Applications. *Polymers* **2017**, *9*, 494. [CrossRef]

36. Bürger, J.; Kunnathully, V.S.; Kool, D.; Lindner, J.K.N.; Brassat, K. Characterisation of the PS-PMMA Interfaces in Microphase Separated Block Copolymer Thin Films by Analytical (S)TEM. *Nanomaterials* **2020**, *10*, 141. [CrossRef]

37. Tseng, Y.-C.; Darling, S.B. Block Copolymer Nanostructures for Technology. *Polymers* **2010**, *2*, 470–489. [CrossRef]

38. Shin, D.O.; Jeong, J.-R.; Han, T.H.; Koo, C.M.; Park, H.-J.; Lim, Y.T.; Kim, S.O. A Plasmonic Biosensor Array by Block Copolymer Lithography. *J. Mater. Chem.* **2010**, *20*, 7241. [CrossRef]

39. Akinoglu, G.E.; Mir, S.H.; Gatensby, R.; Rydzek, G.; Mokarian-Tabari, P. Block Copolymer Derived Vertically Coupled Plasmonic Arrays for Surface-Enhanced Raman Spectroscopy. *ACS Appl. Mater. Interfaces* **2020**, *12*, 23410–23416. [CrossRef] [PubMed]

40. Stamatelatos, A.; Tsarmpopoulou, M.; Geralis, D.; Chronis, A.G.; Karoutsos, V.; Ntemogiannis, D.; Maratos, D.M.; Grammatikopoulos, S.; Sigalas, M.; Poulopoulos, P. Interpretation of Localized Surface Plasmonic Resonances of Gold Nanoparticles Covered by Polymeric Coatings. *Photonics* **2023**, *10*, 408. [CrossRef]

41. Ntemogiannis, D.; Tsarmpopoulou, M.; Stamatelatos, A.; Grammatikopoulos, S.; Karoutsos, V.; Anyfantis, D.I.; Barnasas, A.; Alexopoulos, V.; Giantzelidis, K.; Ndoj, E.A.; et al. ZnO Matrices as a Platform for Tunable Localized Surface Plasmon Resonances of Silver Nanoparticles. *Coatings* **2024**, *14*, 69. [CrossRef]

42. Karoutsos, V. Scanning Probe Microscopy: Instrumentation and Applications on Thin Films and Magnetic Multilayers. *J. Nanosci. Nanotechnol.* **2009**, *9*, 6783–6798. [CrossRef]

43. Moharam, M.G.; Gaylord, T.K. Rigorous Coupled-Wave Analysis of Metallic Surface-Relief Gratings. *J. Opt. Soc. Am. A* **1986**, *3*, 1780. [CrossRef]

44. Tsarmpopoulou, M.; Chronis, A.G.; Sigalas, M.; Stamatelatos, A.; Poulopoulos, P.; Grammatikopoulos, S. Calculation of the Localized Surface Plasmon Resonances of Au Nanoparticles Embedded in NiO. *Solids* **2022**, *3*, 55–65. [CrossRef]

45. Stamatelatos, A.; Tsarmpopoulou, M.; Chronis, A.G.; Kanistras, N.; Anyfantis, D.I.; Violatzi, E.; Geralis, D.; Sigalas, M.M.; Poulopoulos, P.; Grammatikopoulos, S. Optical Interpretation for Plasmonic Adjustment of Nanostructured Ag-NiO Thin Films. *Int. J. Mod. Phys. B* **2021**, *35*, 2150093. [CrossRef]

46. Refractive Index Database. Available online: https://web.archive.org/web/20191229093850/http://polymerdatabase.com/polymer%20physics/Ref%20Index%20Table%20.html (accessed on 21 March 2024).

47. Chronis, A.G.; Stamatelatos, A.; Grammatikopoulos, S.; Sigalas, M.M.; Karoutsos, V.; Maratos, D.M.; Lysandrou, S.P.; Trachylis, D.; Politis, C.; Poulopoulos, P. Microstructure and Plasmonic Behavior of Self-Assembled Silver Nanoparticles and Nanorings. *J. Appl. Phys.* **2019**, *125*, 023106. [CrossRef]

48. Vitos, L.; Ruban, A.V.; Skriver, H.L.; Kollar, J. The surface energy of metals. *Surf. Sci.* **1998**, *411*, 186–202. [CrossRef]

49. Wu, Y.-C.; Wang, L.-W.; Lai, C.-H. Low-temperature ordering of (001) granular FePt films by inserting ultrathin SiO$_2$ layers. *Appl. Phys. Lett.* **2007**, *91*, 072502. [CrossRef]

50. Grammatikopoulos, S.; Pappas, S.D.; Dracopoulos, V.; Poulopoulos, P.; Fumagalli, P.; Velgakis, M.J.; Politis, C. Self-assembled Au nanoparticles on heated corning glass by dc magnetron sputtering: Size-dependent surface plasmon resonance tuning. *J. Nanopart. Res.* **2013**, *15*, 1446. [CrossRef]